*Geotechnical Testing Journal,* Vol. 28, No. 4
Paper ID GTJ12638
Available online at: www.astm.org

*Jong-Sub Lee,*[1] *Americo L. Fernandez,*[2] *and J. Carlos Santamarina*[3]

# S-Wave Velocity Tomography: Small-Scale Laboratory Application

**ABSTRACT:** Arrays of bender elements are combined with simple, yet robust inversion algorithms to develop a device for S-wave tomography. A fixed frame configuration complemented with a new versatile bender element installation permits reducing measurement errors. System design involves optimal selection of transducer separation, a frame design that prevents wave transmission, and an adequate calibration procedure. Reliable tomographic images are obtained by combining data preprocessing and the regularized least squares solution. Given the small size of the data sets, inversion techniques based on a parametric representation of the medium are implemented as well. The tomographic system is tested at low confinement and within a true triaxial cell. Results show the potential of tomographic imaging in the characterization of geotechnical systems and in the monitoring of subsurface processes. In particular, shear wave velocity tomography permits monitoring changes in the velocity field, which is related to the average effective stress in freshly-remolded uncemented soils. A minimum anomaly size and velocity contrast are required for detection. Diffraction healing hinders the detection of low velocity anomalies.

**KEYWORDS:** diffraction healing, inversion, least squares, regularization, parametric representation, pixel representation, spatial coverage, tunnels

## Introduction

Tomography is the determination of the spatial variability of a physical quantity based on the inversion of boundary measurements of chemical, electrical, thermal, or mechanical parameters. Tomography is extensively used in medical diagnosis, including tools such as Computerized Axial Tomography (CAT), Magnetic Resonance Imaging (MRI), and Positron Emission Tomography (PET). Tomographic imaging in the near surface for geotechnical purposes, herein called geotomography, started in ∼1980 (Dines and Lytle 1979; Witten and Long 1986). Wave-based geotomography for near surface applications is typically attempted with the crosshole configuration.

The purpose of this paper is to design a device for high resolution S-wave velocity tomography for small-scale models. Critical concerns include transducer selection and performance, transducer separation, frame characteristics, the selection of robust inversion algorithms to resolve images with limited information, and the development of an adequate calibration procedure. The tomographic system is used to explore the field of stiffness in homogeneous sand specimens subjected to a spatially varying state of stress. This manuscript starts with a review of shear wave propagation in soils and a brief introduction to tomographic inversion.

## Velocity—Stress Relations—Implications

Effective stress governs the shear stiffness of uncemented soils when capillary effects are negligible. The shear wave velocity is dependent on the direction of wave propagation and polarization (Roesler 1979; Knox et al. 1982; Yu and Richart 1984). In terms of effective stresses, the S-wave velocity can be estimated as

$$V_s = \alpha\left(\frac{\sigma'_o}{Pa}\right)^{\beta} = \alpha\left(\frac{\sigma'_p + \sigma'_m}{2Pa}\right)^{\beta} \tag{1}$$

where $\sigma'_o = (\sigma'_p + \sigma'_m)/2$ is the average effective stress on the polarization plane, $\sigma'_p$ is the effective stress in the direction of wave propagation, and $\sigma'_m$ is the effective stress in the direction of particle motion, respectively; $Pa$ is the atmospheric pressure in the same units as $\sigma'_o$, and $\alpha$ and $\beta$ are experimentally determined parameters. The $\alpha$-coefficient and the $\beta$-exponent are interrelated as $\beta = 0.36\text{-}\alpha/700$ (Santamarina et al. 2001). General guidelines for the value of $\beta$ are: $\beta = 0.16 \sim 0.20$ for rounded smooth particles and dense sands, $\beta \approx 0.25$ for loose sands or angular sands, $\beta = 0.3$ for soft clays, and $\beta \leq 0.15$ for over consolidated clays and cemented soils.

The $V - \sigma'_o$ trend measured for a sand used in this study is plotted in Fig. 1*a*. This robust trend suggests that the average effective stress may be inferred from shear wave velocity measurements. However, note that given the nonlinear relationship between velocity and stress, a change in the average stress $\Delta\sigma'_o$ produces a bigger change in velocity $\Delta V_S$ at low confinement than the same stress change $\Delta\sigma'_o$ at higher confinement.

The dependency of the shear wave on state of stress suggests velocity anisotropy in an anisotropic stress field $\sigma'_h = k_o\sigma'_v$. A polar plot of shear wave velocity for F110 sand under $k_o$ stress is shown in Fig. 1*b*. The maximum observed anisotropy is about 7 %.

The straight ray assumption between the source and the receiver is effective (no need for ray tracing) and robust (fewer convergence difficulties). However, rays bend in heterogeneous media according to Snell's law. The S-wave velocity field in the subsurface is inherently vertically heterogeneous and anisotropic ($k_o = \sigma'_h/\sigma'_v \neq 1$), as predicted by Eq 1. For simplicity, consider a linear increase in wave velocity with depth $z$, $V_z(z) = a + bz$ with anisotropy $(c = V_z/V_x,\ V_x = V_y)$ and elliptical wave front $V(\theta) = V_z(z)\sqrt{(1+\tan^2\theta)/(c^2+\tan^2\theta)}$, where a, b and c are constants that characterize the medium, $\theta$ is the angle between

Received April 21, 2004; accepted for publication November 29, 2004; published July 2005.

[1] Postdoctoral Fellow, Civil and Environmental Engineering, Georgia Institute of Technology, Atlanta, GA 30332.

[2] Senior Research Engineer, A. H. Beck Foundation Company, 5123, Blanco Road, San Antonio, TX 78216.

[3] Professor, Civil and Environmental Engineering, Georgia Institute of Technology, Atlanta, GA 30332.

 

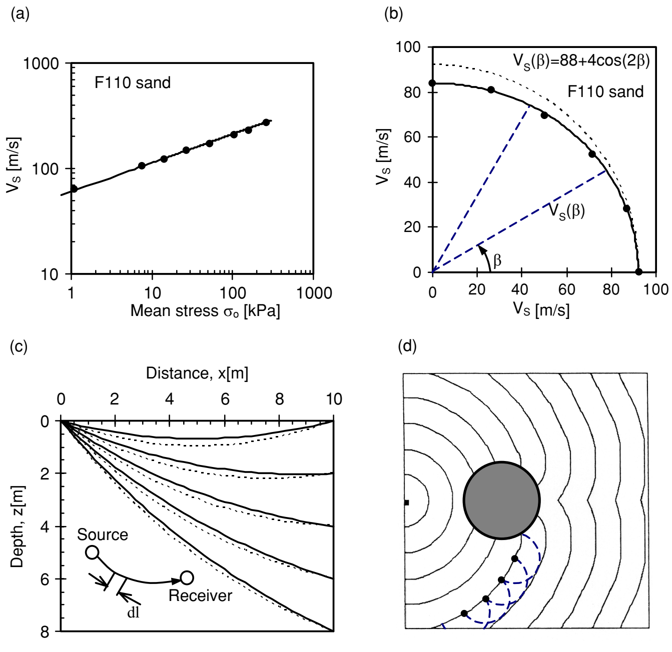


FIG. 1—*Possibilities and difficulties of $V_S$–tomography: (a) Stress dependent shear wave velocity (F110 sand $D_{50} = 0.12$ mm); (b) Stress anisotropy and S-wave velocity anisotropy (F110 sand, $k_o$ state of stress), propagation in $\sigma_3$ direction, particle motion changes from $\sigma_1$ direction $\beta = 0°$ to $\sigma_3$ direction $\beta = 90°$; (c) Ray paths in gradually heterogeneous and anisotropic medium; solid rays: a = 90 m/s, b = 5s$^{-1}$, c = 1 (isotropic medium); dotted rays: a = 90 m/s, b = 5s$^{-1}$, and c = 1.1 (anisotropic medium); (d) Diffraction healing behind a low-velocity inclusion (simulation based on Huygens' wavelets—see Potts and Santamarina 1993).*

the ray and the vertical direction at depth $z$. The equation of the ray path from the source location ($x_s$, $y_s$) to the receiver location ($x_r$, $y_r$) is (Santamarina et al. 2001; see also Hryciw 1989),

$$z(x) = \sqrt{\left(\frac{V_{zs}}{b}\right)^2 + (x - x_s)\left[\frac{V_{zr}^2 - V_{zs}^2}{b^2(x_r - x_s)} + c^2(x_r - x)\right]} - \frac{a}{b} \tag{2}$$

where $V_{zr}$ and $V_{zs}$ are the vertical velocities at receiver and source locations. Ray paths for typical near-surface soil parameters are presented in Fig. 1*c*. The travel time is numerically integrated along the ray path (Equation 2).

$$t = \int_S^R \frac{1}{V(\theta)} \mathrm{dl} = \int_S^R \frac{\sqrt{1 + \tan^2\theta}}{V(\theta)} \mathrm{dx} \approx \sum_{x_s}^{x_r} \frac{\sqrt{1 + \tan^2\theta}}{a + bz} \Delta x \tag{3}$$

where $\mathrm{dl} = \mathrm{dx} \cdot \sqrt{1 + \tan^2\theta}$ is the differential of the ray length along the ray slope θ. Equations 2 and 3 permit inverting the unknown heterogeneity (a, b) and anisotropy (c) parameters from tomographic data. In addition, they allow performing simulation studies to optimize the system design in order to minimize the effects of non-linearities inherent to ray bending.

"Diffraction healing" hinders the detection of low velocity anomalies (Fig. 1*d*). This phenomenon is readily understood from Huygens' principle: every point on a wave front is the source of new wavelets; the new position of the wave front after $\Delta t$ is determined by the envelope of these wavelets. As shown in Fig. 1*d*, wave fronts close and heal after a low velocity anomaly, gradually hiding its presence.

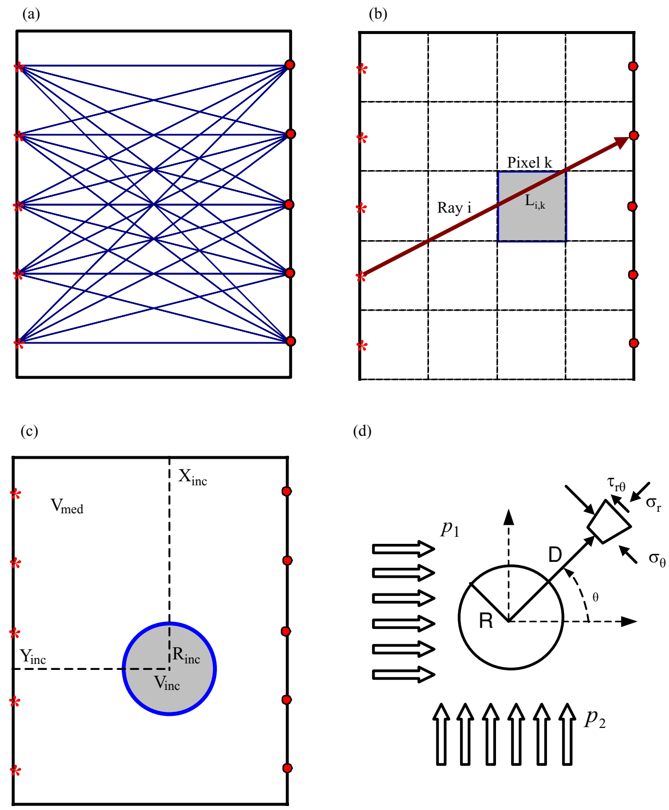


FIG. 2—*Tomographic imaging: (a) Ray paths for crosshole tomography, (b) Pixel based representation, (c) Parametric based representation of an anomaly in a homogeneous background, (d) Parametric based representation of an axisymmetric stress field.*

## Tomographic Software: Fundamental Concepts

Tomographic inversion can be based on a pixel-based representation or a parametric based representation of the unknown space (Fig. 2). The following review of these two implementations is based on inversion concepts and methods proposed for limited data sets in Santamarina and Fratta (1998) and Prada et al. (2000). More general reviews can be found in Menke (1998) and Tarantola (1987).

### *Pixel Based Representation*

The travel time $t_i$ along the ith ray is the summation of the travel length $L_{i,k}$ in pixel $k$ times the slowness $S_k$ (Fig. 2*b*)

$$t_i^{\langle \text{meas} \rangle} = \sum_k L_{i,k} \cdot S_k \tag{4}$$

This can be expressed in matrix form for all rays $\boldsymbol{t} = \boldsymbol{L} \cdot \boldsymbol{S}$, where $\boldsymbol{t}_{[m\times1]}$ is the array of measured travel times, $\boldsymbol{L}_{[m\times n]}$ is the matrix of the estimated pixel travel lengths, $\boldsymbol{S}_{[n\times1]}$ is the array of the unknown pixel slowness, $m$ is the number of the measurements, and $n$ is the number of the unknowns.

The goal of inversion is to determine the unknown pixel slownesses $\boldsymbol{S} = \boldsymbol{L}^{inv} \cdot \boldsymbol{t}$, where $\boldsymbol{L}^{inv}$ is a generalized inverse of the matrix of travel lengths. Generally, crosshole tomography is a mix-determined problem due to limited illumination angles. The regularized least-squares solution overcomes ill-conditioning in mix-determined problems:

$$\boldsymbol{S} = (\boldsymbol{L}^T \cdot \boldsymbol{L} + \lambda \boldsymbol{R}^T \cdot \boldsymbol{R})^{-1} \cdot \boldsymbol{L}^T \cdot \boldsymbol{t} \tag{5}$$

where $\lambda$ is the non-negative regularization coefficient (when $\lambda = 0$, the least-squares solution is obtained) and $\boldsymbol{R}$ is the regularization matrix which is after based on Laplacian smoothing. The optimal value of $\lambda$ is obtained by plotting the minimum and maximum values of computed pixel velocities together with the norm of the residuals $\boldsymbol{e}^T \cdot \boldsymbol{e}$ for different values of $\lambda$, where the residual $\boldsymbol{e}^T \cdot \boldsymbol{e}$ is

$$\boldsymbol{e}^T \cdot \boldsymbol{e} = (\boldsymbol{t} - \boldsymbol{L} \cdot \boldsymbol{S})^T \cdot (\boldsymbol{t} - \boldsymbol{L} \cdot \boldsymbol{S}) \tag{6}$$

An example is presented later in this study.

### *Parametric Based Representation*

Pixel based solutions typically involve a large number of unknowns "$n$," weakening invertibility, and increasing variance (For example, if the medium is discretized into $20 \times 20$ pixels, there are $n = 400$ unknowns). Alternatively, the medium and the anomaly may be parametrically described in terms of some global characteristics. Parametric characterization is case specific. Two examples follow. The first example consists of a circular anomaly in a homogeneous background (Fig. 2*c*). There are five unknowns: the velocity of medium $V_{med}$ and the velocity $V_{inc}$, size $R_{inc}$, and location $X_{inc}$, $Y_{inc}$ of the anomaly or inclusion. The second example is related to the velocity field around a pressurized cavity within a soil mass subjected to a $k_o$- far field stress condition. Because stiffness and average stress can be related through Eq 1, the medium can be captured in terms of the following parameters (Fig. 2*d*): the far field stresses, the internal pressure of the inclusion, its size and location. The selected stress function has two components:

1. A first-order Fourier series approximation to solve for the stress field around a circular cavity in an biaxially loaded homogeneous medium;
2. An axisymmetric stress field induced by the pressurized inclusion (Fig. 2*d*).

Without the intent to presume elasticity, the selected function resembles the Kirsch-type solution (Poulos and Davis 1974; Goodman 1989):

$$\sigma'_r = P_{int}\left(\frac{R^2}{D^2}\right) + \left(\frac{p_1 + p_2}{2}\right)\left(1 - \frac{R^2}{D^2}\right) + \left(\frac{p_1 - p_2}{2}\right)\left(1 - \frac{4R^2}{D^2} + \frac{3R^4}{D^4}\right)\cos 2\theta \tag{7}$$

$$\sigma'_\theta = -P_{int}\left(\frac{R^2}{D^2}\right) + \left(\frac{p_1 + p_2}{2}\right)\left(1 + \frac{R^2}{D^2}\right) - \left(\frac{p_1 - p_2}{2}\right)\left(1 + \frac{3R^4}{D^4}\right)\cos 2\theta \tag{8}$$

Note that cavity expansion solutions provide similar trends for the first component (see Borden and Yan 1989).

When the medium is represented in parametric form, inversion consists of searching by successive forward simulations for the set of model parameters that minimizes the error norm between the measured $\boldsymbol{t}$ and the calculated $\boldsymbol{t}^{\langle calc \rangle}$ travel times. The step-by-step inversion procedure includes:

1. Estimate the initial values of the unknowns from data preprocessing results,
2. Compute the travel time for all $N$ rays $\boldsymbol{t}^{\langle calc \rangle}$,
3. Compute the residuals $e_i + (t_i^{\langle calc \rangle} - t_i)$ where $t_i^{\langle calc \rangle}$ is the calculated $i$th travel time and $t_i$ is the $i$th travel measured time,
4. Evaluate the norm of the residual,
5. Perturb one model parameter and repeat from Step 2.

The norm of the residual or error norm is computed as

$$E = \left(\sum_{i=1}^{m} |e_i|^u\right)^{\frac{1}{u}} \tag{9}$$

where $m$ is the number of the measurements. Typically, $u = 2$ and the least-square solution is obtained. However, given the uneven distribution of information in crosshole tomography, the $u = \infty$ norm may be used when low-noise data are available.

## Tomographic Hardware: Transducers, Frame, Calibration

Bender elements are convenient shear wave transducers due to their optimal coupling to the soil mass. In this application, piezoelectric bender elements are installed on a rigid frame to reduce measurement errors. The frame is calibrated using a Plexiglas plate. Details follow.

### *Transducers*

Series bender elements are connected to coaxial cables, coated in polyurethane, and anchored into Nylon screws with epoxy resin (see insert Fig. 3). This choice of materials and installation minimizes vibration transmission into the frame, facilitates the modular construction of the tomographic device, allows for easy replacement of malfunctioning transducers, and permits rotating the transducer to explore conditions with alternative polarization. The cantilever length of the bender element is 6 mm. The width and thickness of bender element used are 8 mm and 0.6 mm, respectively. The characteristic frequency ranges between 6 and 9 kHz. Extensive details on bender element installation and performance, including central frequency and directivity, can be found in Lee and Santamarina (2004).

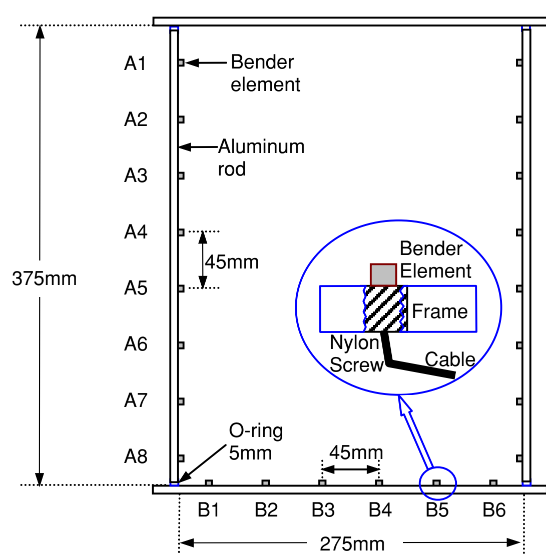


FIG. 3—*Tomographic hardware–transducer installation within readily replaceable anchors, and supporting frame.*

*Tomographic Frame*

*Dimension*—The frame that houses the bender elements is presented in Fig. 3. The geometry is designed to optimize various physical criteria, such as skin depth (the penetration distance of a plane wave until its amplitude decays to $1/e$ the initial amplitude), resolution, information content, source directivity, and ray curvature (Fernandez and Santamarina 2003). The center-to-center separation between consecutive bender elements is 45 mm, and it is selected to balance resolution requirements, information duplication (Fresnel's ellipse), and travel time resolution.

*Frame Connection*—The vibration generated at a source is also transmitted through the frame and may reach the receivers affecting the detection of the wave fronts traveling through the soil mass. Several methods are investigated to mechanically filter frame transmission. The simplest and most effective method is to fix the sides of the frame with nylon bolts and to separate the metallic sides with O-rings. Furthermore, the amplitude of the transmitted vibration decreases dramatically when a single-cycle sine wave is used as input as compared with step input signal when the characteristic period of bender element (and the input sine) is significantly different from the resonant period of the buried frame.

*Spatial Coverage and Information Content*—A large number of rays does not necessarily imply an over-determined condition, since some measurements may be linearly dependent and do not contribute additional information. The total length traveled by all the rays in each pixel is a simple estimate of the spatial distribution of information in the cross section to be resolved. Figure 4*a* shows the ray paths, and Fig. 4*c* shows travel lengths per pixel for the crosshole configuration. When needed, bender elements can be installed in the bottom and top sides of the frame to enhance the information content in the upper and lower regions. The effect of adding

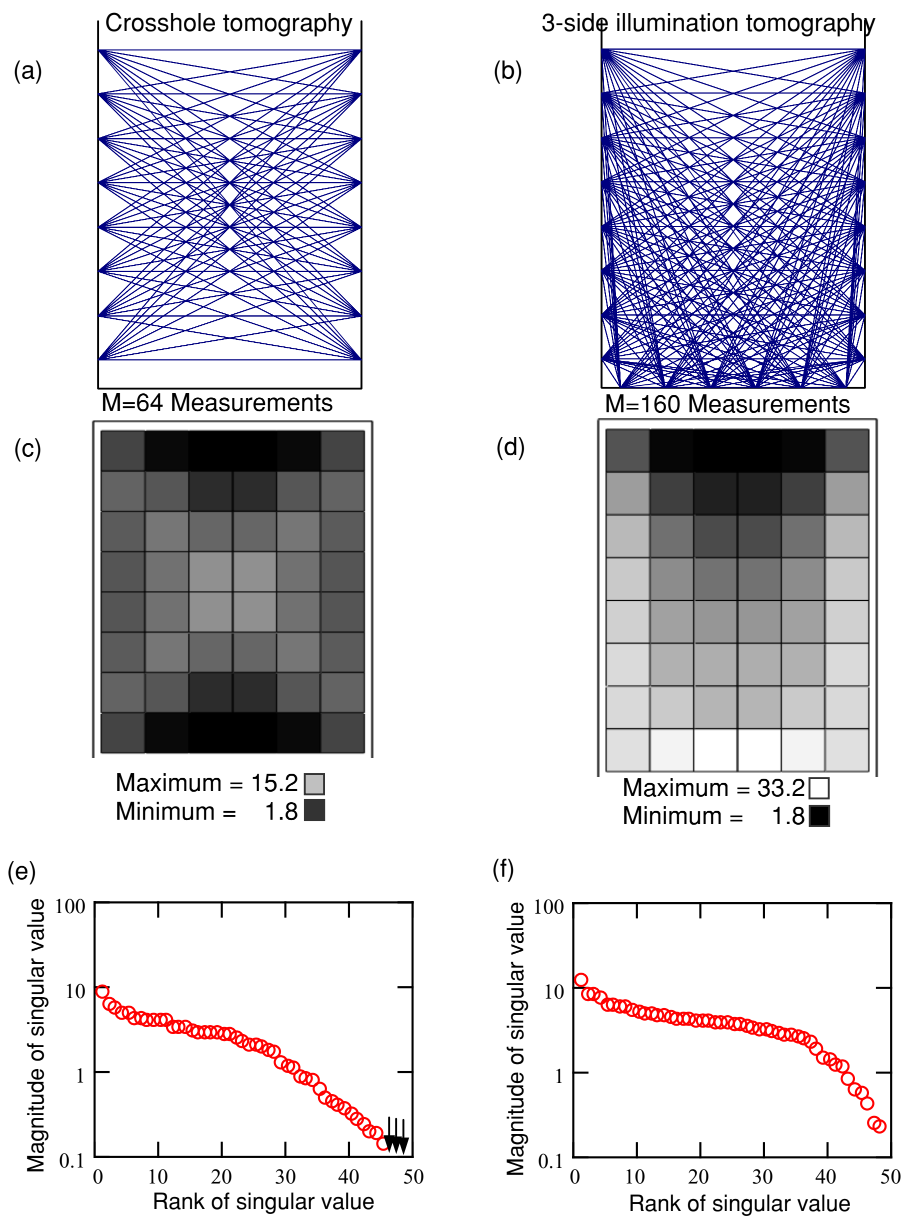


FIG. 4—*Data preprocessing–comparison between crosshole tomography and 3-side illumination tomography; (a) & (b) ray paths; (c) & (d) spatial coverage, the total traveled length in each pixel is normalized with respect to the pixel width (43.8 mm); (e) & (f) singular values; same number of pixels: $N = 48$.*

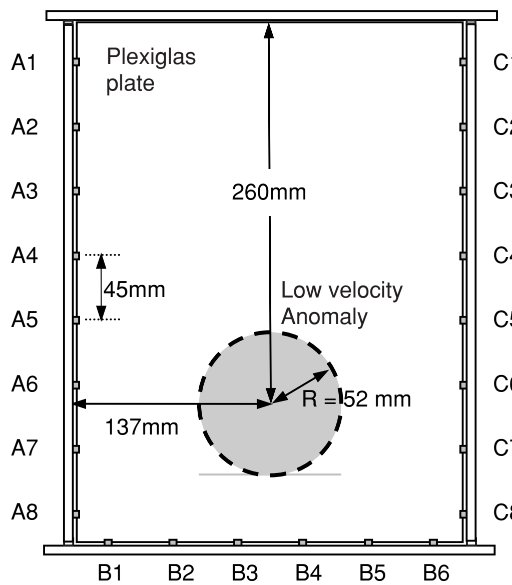


FIG. 5—*Calibration; plexiglas plate dimension: 365 × 270 × 3 (length × width × thickness in mm).*

bender elements on the lower part of the frame on the distribution of information content is shown in Figs. 4*b* and 4*d*. Clearly, the "crosshole" configuration covers the central zone best, while the "3-side illumination" case produces high coverage in the central and lower part of the cross section. The number of independent equations may be assessed by singular value decomposition (the number of meaningful eignevalues in the transformation—details in Golub and Van Loan 1996). Figures 4*e* and 4*f* show the singular values for crosshole and 3-side illumination tomography. The ratio between the largest and the smallest singular value or "condition number" is $3.8 \times 10^8$ in crosshole and 54 in 3-side illumination. Therefore 3-side illumination leads to a significantly better conditioned inversion problem.

### *Calibration with Plexiglas Plate*

The frame-based tomographic system has two main advantages. First, transducer positioning errors are minimized. Second, the system can be calibrated before burying it in the soil mass. A simple calibration procedure is presented next.

*Description*—The calibration technique explored herein uses a Plexiglas plate (thickness 3 mm) that rests on the transducers (vacuum grease was added to ensure coupling—Fig. 5), and transmitted Lamb waves. After calibration with a homogeneous plate, the critical case of a low velocity anomaly (diffraction healing) is tested by cutting a hole of radius $R_{inc} = 52$ mm in the plate. A single cycle input sine wave is used to minimize vibration transmitted along the frame.

*Data Preprocessing*—Travel times versus ray lengths are plotted in Fig. 6. The trend approaches a straight line in the case of the plate without anomaly. The slope is the inverse of the Lamb wave velocity. The measured value $V_L \approx 625$ m/s matches the analytical solution based on $V_P = 2360$ m/s, $V_S = 1370$ m/s, and $f = 9$ kHz (solution in Achenbach 1973; Graff 1975). Deviations from the straight line indicate measurement errors: the mean error in travel time is 8.3 μs (∼2.3 % of the travel time) with a standard deviation of 6.9 μs (see Fig. 6). In the case of the plate with a hole, measurements above the straight line denote the presence of the anomaly.

*Inversion*—For completeness, pixel- and parametric-based representations are implemented to obtain tomographic images of the low velocity anomaly in the Plexiglas plate. Both methods are applied using crosshole data and 3-side illumination data. Straight rays are assumed to obtain the first estimate of the velocity field. The regularized least square solution (Eq 5) is computed with the regularization matrix based on Laplacian smoothing. The regularization coefficient λ is selected by taking into consideration trends in the residual (Eq 6) and the trends in maximum and minimum pixel values as shown in Fig. 7*a*. If λ is low, the residual $[e]^T[e]$ is low, and the data is properly justified; however, measurement and model errors become magnified in the solution, and computed pixel values may lose physical meaning. On the other hand, when λ is high, the image becomes homogeneous, i.e., uninformative, and the increase in the residual indicates that the data are not properly considered in the solution. For this study, a regularization coefficient $\lambda = 3$ renders adequate images for both the crosshole and 3-side illumination data (Figs. 7*b* and 7*c*). The images yield the location of the anomaly; however, the velocity of the anomaly is not zero due to the imposed straight ray assumption.

Inversion based on the parametric representation involves the five unknowns $V_{med}$, $V_{inc}$, $R_{inc}$, $X_{inc}$, and $Y_{inc}$. Results are plotted in Fig. 8. Several observations follow:

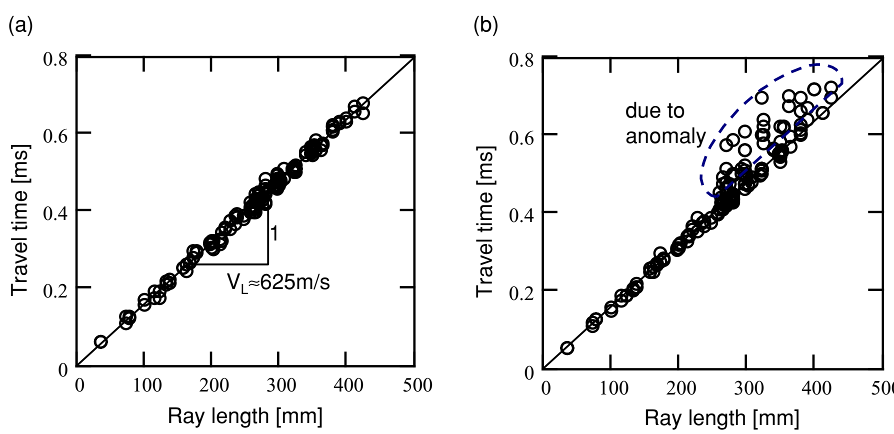


FIG. 6—*Calibration tests–data preprocessing (3-side illumination data): Travel time versus ray length: (a) Without anomaly; the small deviations from the straight line indicate measurement errors: mean error 8.3 μs (∼2.3 %) and standard deviation 6.9 μs. (b) With anomaly; the large deviations from the straight line denote the presence of the low velocity anomaly.*

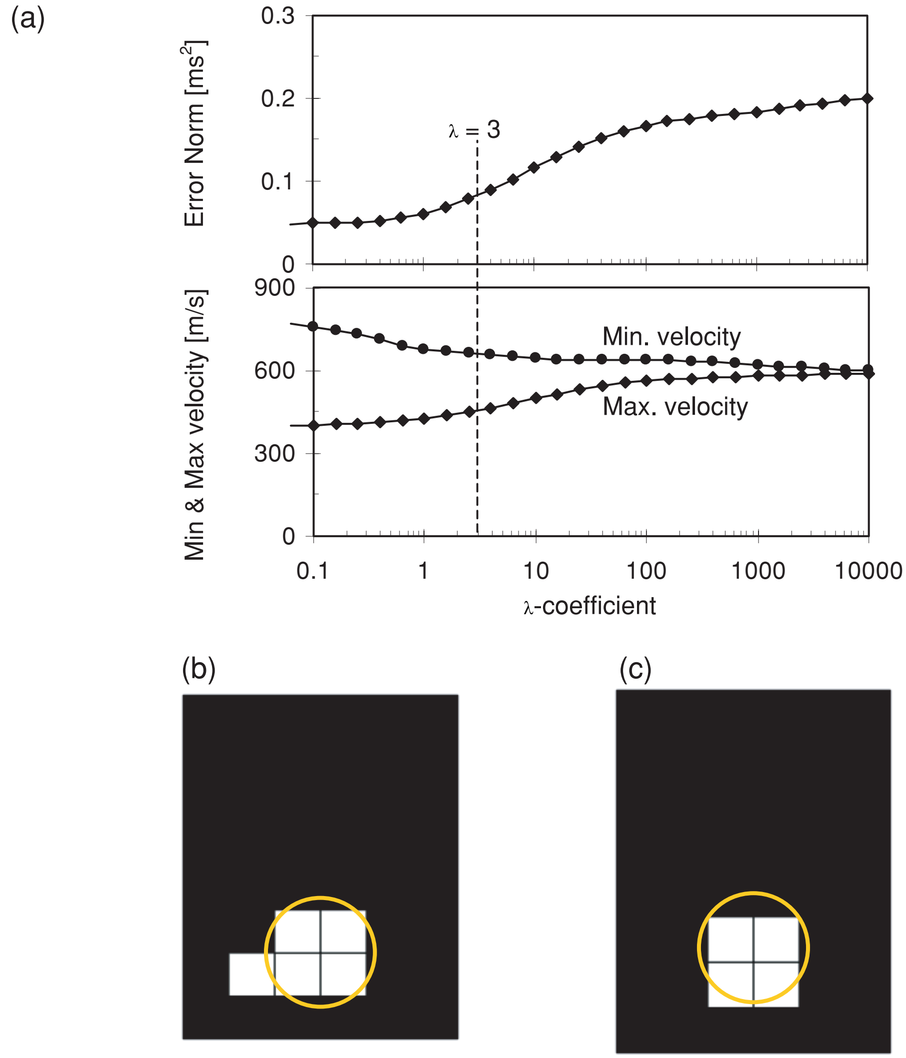


FIG. 7—*Calibration study; (a) selection of the λ coefficient for RLSS in 3-side illumination tomography—Error norm and extreme pixel values versus regularization coefficient; (b) thresholded tomographic image for crosshole illumination; (c) thresholded tomographic image for 3-side illumination; both images obtained with* $\lambda = 3$*; Pixel width: 43.8 mm.*

1. The two illumination methods produce good convergence for all unknown parameters,
2. The 3-side illumination tomography yields larger error norm than the crosshole tomography because there are more measurements considered in the summation—Eq 9,
3. The convergence of $X_{inc}$ and $Y_{inc}$ is better defined in 3-side illumination,
4. The error norm of the Y-coordinate (Fig. 8*b*) is steeper than that of the X-coordinate (Fig. 8*a*), especially in 3-side illumination (analyzed in Santamarina and Reed 1994),
5. The inverted radius is slightly smaller than the real size in both illumination cases due to diffraction healing,
6. The inferred non-zero velocity of the anomaly reflects the straight ray assumption (Fig. 8*e*).

*Installation*

The frame is placed within the chamber where the experiment will be conducted either at 1 g or at N · g (geotechnical centrifuges); chambers include zero-lateral strain boxes, true triaxial cells, and shear boxes. Then, the soil is placed following standard procedures such as dry pluviation, vibration densification, or water sedimentation. It is anticipated that the presence of the frame perturbs the system during specimen preparation and during testing. However, the information density for the selected configuration focuses on the central region away from the frame boundaries (Figs. 4*c* and 4*d*).

**Geotomography—Examples**

Several unique tomographic studies are implemented using two similar prototypes of the hardware, and the inversion techniques described above. Travel times are computed with hand-picked first arrivals, but looking at the complete fan of measurements from a given source rather than operating on a single trace at the time. This approach overcomes difficulties associated with signatures gathered at high angularity with respect to the directivity of the transducers. Measurements are not affected by near-field effects for the selected frame geometry and operating frequencies. In all cases, travel times $t_i$ are 7–18 times the characteristic period $T$ in the signal resulting in an estimated measurement error $(T/8)/t_i \approx 2\,\%$.

The velocity field is determined by the imposed stress field. Tests include a layered stress field and a pressurized internal anomaly.

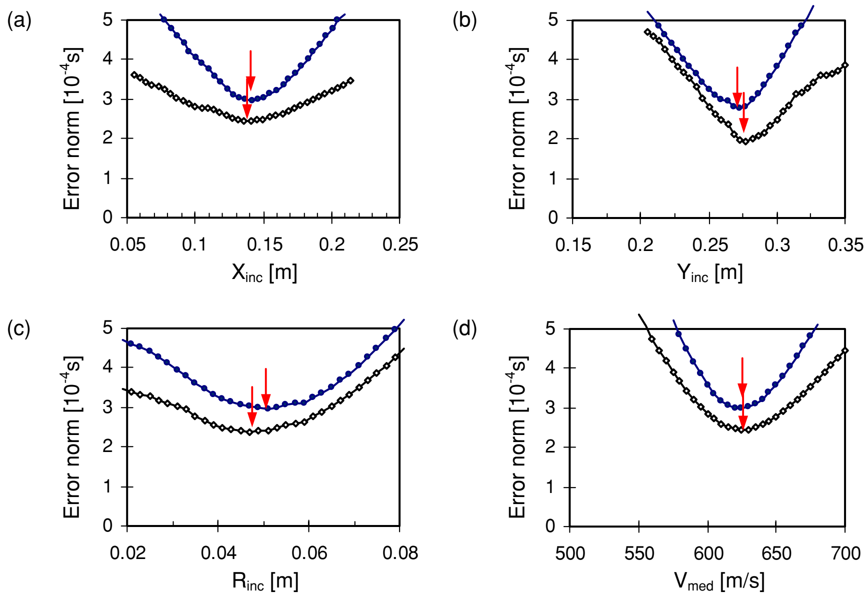


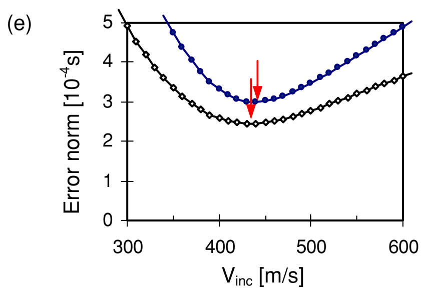


(f)

| | True | Cross (◊) | 3-side (•) |
|---|---|---|---|
| $X_{inc}$ [m] | 0.138 | 0.140 | 0.142 |
| $Y_{inc}$ [m] | 0.260 | 0.277 | 0.270 |
| $R_{inc}$ [m] | 0.052 | 0.046 | 0.050 |
| $V_{med}$ [m/s] | 625 | 625 | 625 |
| $V_{inc}$ [m/s] | 0 | 430 | 440 |

FIG. 8—*Paametric inversion–Slices of error surface; comparison between crosshole and 3-side illumination tomography; (a) inclusion X-coordinate; (b) inclusion Y-coordinate; (c) radius of inclusion; (d) velocity of medium; (e) velocity of inclusion; (f) summary of parametric inversion results.*

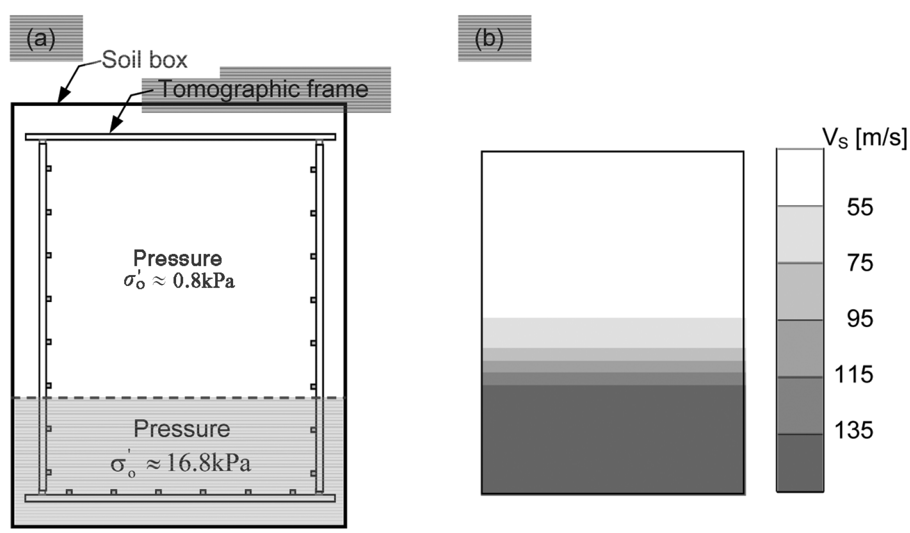


FIG. 9—*Low and high velocity regions; (a) Test configuration; Soil box dimension: 470 × 440 × 170 Length × Width × Depth in mm; uniform pressure is applied in the lower part of the frame; F110 sand; (b) Pixel based representation—tomographic images obtained with the regularized least squares solution; Pixel width: 43.8 mm.*

*Layered Stress Field*

The first geotomography test is performed at 1 g in a soil box 470 mm long, 440 mm wide, and 170 mm deep. A uniform sand specimen is prepared by dry pluviation using F110 sand ($D_{50} = 0.12$ mm, $C_c = 0.99$, and $C_u = 1.6$. see Fig. 1*a*). The tomographic frame is installed in the middle of the soil layer on the horizontal plane, with in-plane bender elements. Consequently, the direction of S-wave propagation is the direction of the horizontal stress and the direction of the particle motion is the direction of the vertical stress. A uniform pressure is applied in the lower part of the frame as shown in Fig. 9*a*. Figure 9*b* shows the tomographic image obtained by the regularized least squares solution using a horizontal

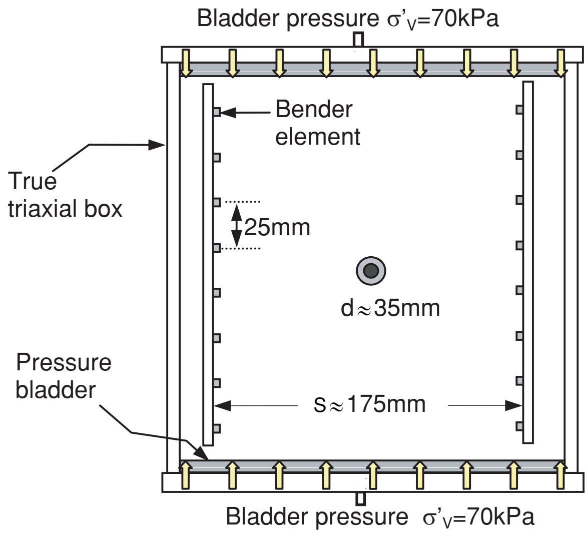


FIG. 10—*Setup for S-wave velocity tomographic imaging within a true triaxial device—anomaly detection; $k_o$ state of stress.*

smoothing criterion, i.e., the second horizontal derivative is minimized in the horizontal direction and rows in the regularization matrix are computed with the [1, –2, 1] kernel. This criterion is particularly relevant to near surface soil conditions where the high stress gradient tends to control the spatial distribution of stiffness.

Results in Fig. 9*b* readily show the high velocity zone in the lower part of the tomogram (for further details, see Lee 2003). Inverted velocities are in agreement with the applied stress and the velocity-stress response for this sand (Fig. 1*a*).

### *Pressurized Anomaly—True Triaxial Device*

A well-controlled stress field is attained in the true triaxial box shown in Fig. 10. The far field boundary stresses are imposed with bladders on the walls of the true triaxial cell. The tomographic hardware is installed within the true triaxial box. In this case, two vertical arrays of eight bender elements are installed in crosshole tomographic configuration. An inflatable cylinder is buried during dry pluviation; this device consists of tube perforated along its length and surrounded by a very flexible latex sleeve. This is a pressure-controlled boundary, and it resembles many field conditions such as lifelines, tunnels, trenchless excavations, and penetrometers used for in situ testing. The ratio between transducer separation $S$ and tunnel diameter $d$ is $S/d \approx 5$. Crushed sand is used in this study ($D_{50} = 0.32$ mm, $C_c = 0.98$, and $C_u = 2.1$). The complete dataset and results can be found in Fernandez (2000).

The inversion results obtained with the pixel based representation for 70 kPa vertical effective stress (average effective stress on polarization plane $\sigma'_o = 50$ kPa) and 140 kPa inclusion pressure are presented in Fig. 11*a*. The high velocity zone is clearly detected. The inversion based on parametric-based representation is performed using Eqs 7 and 8. The convergence of the inverted internal pressure of the anomaly is shown in Fig. 11*b*.

In general, adequate tomographic images are obtained when the pressure in the inclusion is greater than the applied far field vertical stress. Furthermore, very small inclusions are not detected even when they are subjected to high pressure. Detectability can be assessed by estimating the ratio between the travel times with and without the inclusion. Consider a source-to-receiver distance $L_b$ in a medium of velocity $V_{med}$ and an inclusion of diameter $d_{inc}$ and velocity $V_{inc}$ (Fig. 12*a*). Then, the relative change in travel time due to the presence of the inclusion is:

$$\frac{\delta t}{t_{wo}} = \frac{t_w - t_{wo}}{t_{wo}} = \frac{\frac{L_b - d_{inc}}{V_{med}} + \frac{d_{inc}}{V_{inc}}}{\frac{L_b}{V_{med}}} - 1 = \frac{d_{inc}}{L_b}\left(\frac{V_{med}}{V_{inc}} - 1\right) \quad (10)$$

where $t_w$ and $t_{wo}$ are the travel times with and without the inclusion, respectively. The value of $\delta t$ must exceed the precision in travel time measurements $\varepsilon_t$. Figure 12*b* shows contour lines of normalized change in travel time. The range of anomaly characteristics, in terms of $V_{inc}/V_{med}$ and $d_{inc}/L_b$, where detection is not possible is highlighted for a precision in travel time measurements of $\varepsilon_t = 2.3\,\%$ (as observed in Fig. 6).

## Conclusions

The design, calibration, and application of S-wave velocity tomography for small-scale laboratory tests are documented in this study. The geometry of the tomographic device must be accurately defined to reduce measurement errors, which are magnified during inversion. Several factors should be considered in the design of the tomographic hardware including transducer directivity, transducer separation, time resolution, information content, and spatial coverage. Waves transmitted through the frame must be mechanically filtered to avoid data interference.

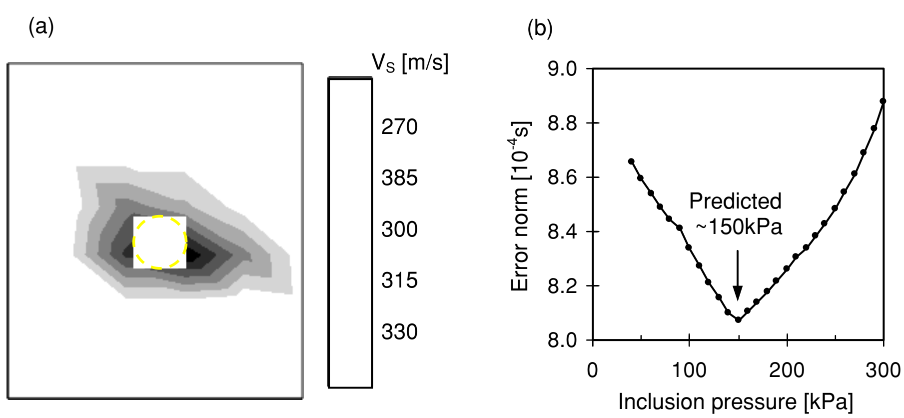


FIG. 11—*S-wave velocity tomographic images within the true triaxial device; $\sigma'_v = 70$ kPa ($\sigma'_o = 50$ kPa); $P_{inc} = 140$ kPa; (a) Pixel based inversion—contour image (thresholded below 270 m/s); (b) Error norm of inclusion pressure from parametric based representation.*

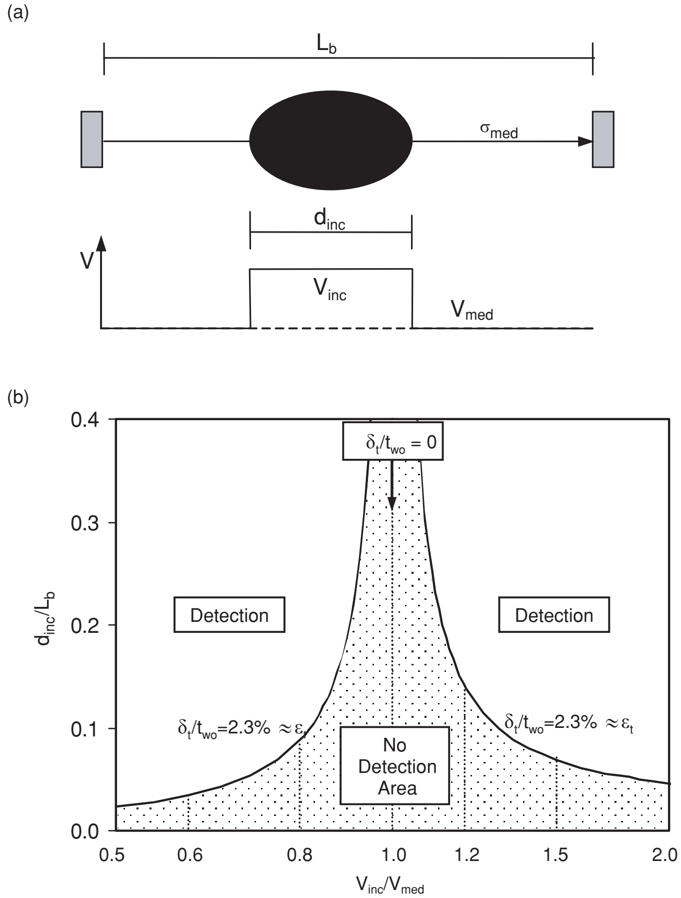


FIG. 12—*Anomaly detection; (a) Assumed geometry and velocities; (b) Minimum size and velocity contrast for travel-time based detection; the NO Detection Area is bounded for travel time precision* $\varepsilon_t = 2.3\,\%$.

The regularized least squares solution is a robust algorithm for pixel-based tomographic imaging. While parametric-based representation requires successive forward simulations, it involves a smaller set of unknowns and renders reliable convergence in crosshole tomography as well as in 3-side illumination tomography.

Shear wave tomography permits monitoring the field of average-stress in freshly remolded-uncemented soils. Anomaly size and contrast must cause changes in travel time that exceed measurement errors. Diffraction healing hinders the detection of low velocity anomalies.

*Acknowledgment*

This study was supported by the NSF-NEES project (based at the University of California at Davis and directed by Dr. B. L. Kutter), PDVSA-Intevep, and The Goizueta Foundation.

## References

Achenbach, J. D., 1973, *Wave Propagation in Elastic Solids*, North-Holland.

Borden, R. H. and Yan, S. L., 1989, "Axial Capacity of Pressure-Injected Piles: A Cavity Expansion Model," *Foundation Engineering: Current Principles and Practices*, *ASCE Geotechnical Special Publication No. 22*, pp. 1505–1519.

Dines, K. and Lytle, J., 1979, "Computerized Geophysical Tomography," *Proceedings of Institute of Electrical and Electronics Engineers*, Vol. 67, No. 8, pp. 1065–1073.

Fernandez, A., 2000, "Tomographic Imaging the State of Stress," PhD Thesis, Georgia Institute of Technology, Atlanta, GA.

Fernandez, A. and Santamarina, J. C., 2003, "Design Criteria for Geotomographic Field Studies," *Geotechnical Testing Journal*, Vol. 26, No. 4, pp. 1–11.

Golub, G. H. and Van Loan, C. F., 1996, *Matrix Computations*, 3rd ed., John Hopkins University Press.

Goodman, R. E., 1989, *Introduction to Rock Mechanics*, 2nd ed., John Wiley and Sons, New York.

Graff, K. F., 1975, *Wave Motion in Elastic Solids*, Dover Publications.

Hryciw, R. D., 1989, "Ray-Path Curvature in Shallow Seismic Investigations," *Journal of Geotechnical Engineering*, Vol. 115, No. 9, pp. 1268–1284.

Knox, D. P., Stokoe, K. H., II., and Kopperman, S. E., 1982, "Effect of State of Stress on Velocity of Low-Amplitude Shear Waves Propagating along Principal Stress Directions in Dry Sand," *Geotechnical Engineering Report GR 82-23*, University of Texas at Austin.

Lee, J. S., 2003, "High Resolution Geophysical Techniques for Small-Scale Soil Model Testing," PhD Thesis, Georgia Institute of Technology, Atlanta, GA.

Lee, J. S. and Santamarina, J. C., 2004, "Bender Elements: Performance and Signal Interpretation,"*Journal of Geotechnical and Geoenvironmental Engineering* (Submitted).

Menke, W., 1998, *Geophysical Data Analysis: Discrete Inverse Theory*, Academic Press.

Potts, B. D. and Santamarina, J. C., 1993, "Geotechnical Tomography: The Effect of Diffraction," *Geotechnical Testing Journal*, Vol. 16, No. 4, pp. 510–517.

Poulos, H. G. and Davis, E. H., 1974, *Elastic Solutions for Soil and Rock Mechanics*, John Wiley and Sons.

Prada, J., Fratta, D., and Santamarina, J. C., 2000, "Tomographic Detection of Anomalies with Limited Data Sets—Velocity and Attenuation," *Geotechnical Testing Journal*, Vol. 23, No. 4, pp. 472–486.

Roesler, S. K., 1979, "Anisotropic Shear Modulus Due to Stress Anisotropy," *Journal of Geotechnical Engineering*, Vol. 105, No. 7, pp. 871–888.

Santamarina, J. C. and Fratta, D., 1998, *Introduction to Discrete Signals and Inverse Problems in Civil Engineering*, ASCE Press, VA.

Santamarina, J. C. and Reed, A. C., 1994, "Ray Tomography: Errors and Error Functions." *Journal of Applied Geophysics*, Vol. 32, pp. 347–355.

Santamarina, J. C., Klein, K. A., and Fam, M. A., 2001, *Soils and Waves—Particulate Materials Behavior, Characterization and Process Monitoring*, John Wiley and Sons, New York.

Tarantola, A., 1987, *Inverse Problems Theory*, Elsevier.

Witten, A. J. and Long., E., 1986, "Shallow Application of Geophysical Diffraction Tomography," *IEEE Transactions on Geoscience and Remote Sensing*, Vol. 24, No. 5, pp. 654–662.

Yu, P. and Richart, F. E., Jr., 1984, "Stress Ratio Effects on Shear Modulus of Dry Sands," *Journal of Geotechnical Engineering*, Vol. 110, No. 3, pp. 331–345.